A dual interpolation boundary face method with Hermite-type approximation for potential problems

Jianming Zhang*, Rui He, Baotao Chi, Weicheng Lin

State Key Laboratory of Advanced Design and Manufacturing for Vehicle Body, College of Mechanical and Vehicle Engineering, Hunan University, Changsha 410082, China

ABSTRACT

This paper presents the dual interpolation boundary face method combined with a Hermite-type moving-least-squares approximation for solving complex two-dimensional potential problems. Compared to the standard algorithms, this combined method is better suited for structures with small feature sizes such as short edges and small chamfers. The interpolation functions, if constructed in cyclic coordinates, making it difficult to apply this new method to deal with complex structures with small feature sizes in which only one source point is assigned. The Hermite-type approximation formulated in Cartesian coordinates is able to completely overcome this obstacle by searching for source points on adjacent edges. Additionally, an improved and incomplete quadratic polynomial basis is presented to obtain an accurate algorithm for the Hermite-type approximation. We use several numerical examples to demonstrate the high accuracy and efficiency of the proposed method for solving various engineering structures with small feature sizes.

© 2020 Elsevier Inc. All rights reserved.

1. Introduction

The boundary integral equation (BIE), or boundary element method (BEM), is a powerful numerical tool applicable to almost all fields of engineering [1–4]. The BEM reduces the original problem by one dimension and does not require continuity of the trial functions. Therefore, it can use both continuous and discontinuous elements [5–7], alleviating the difficulties in mesh generation. To avoid geometric errors in the BEM, Zhang [8,9] developed the boundary face method (BFM) in which the integrand quantities are calculated directly from curves rather than elements.

The continuous and discontinuous elements have both advantages and disadvantages [10,11]. Recently, Zhang [12,13] presented the dual interpolation boundary face method (DiBFM). Its dual interpolation element can unify the continuous and discontinuous elements, and there are two kinds of nodes: source and virtual. The BIEs are collocated at the source nodes, meaning the degrees of freedom for all virtual nodes are condensed by the second-layer interpolation, in this case a standard moving-least-squares (MLS) approximation. Hereafter, we refer to the DiBFM combined with the MLS approximation as DiBFM-MLS.

Lancaster and Salkauskas [14] proposed the MLS approximation. For boundary-only problems, the interpolation functions are constructed in the cyclic coordinates rather than Cartesian coordinates, because the moment matrix in the latter coordinates is singular when all interpolation points lie along a straight line. As a result, the support domain of a virtual node must be restricted to the corresponding edge in 2-D problems (see Fig. 1(a)). It is difficult for the DiBFM-MLS to handle

---

* Corresponding author.
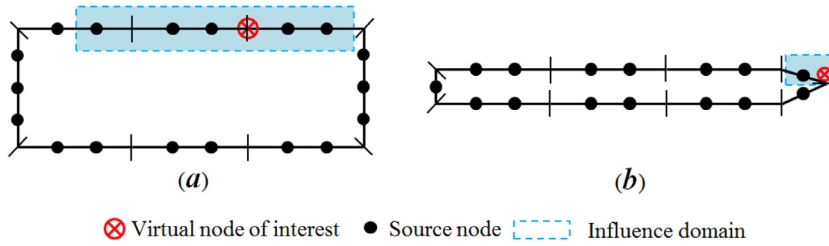 *E-mail address:* zhangjm@hnu.edu.cn (J. Zhang).

Fig. 1. Influence domain of a virtual point in the standard MLS approximation: (a) virtual point is on an edge; (b) virtual point is at a vertex.
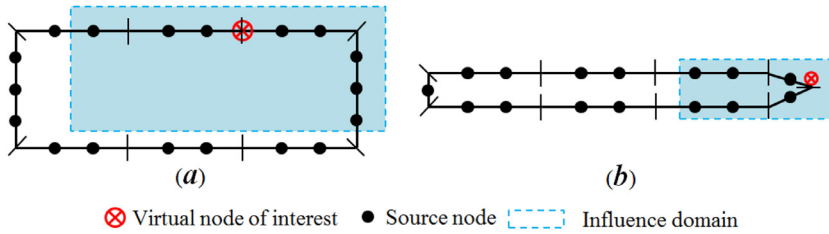

Fig. 2. Influence domain of a virtual point in the HMLS approximation: (a) virtual point is on an edge, (b) virtual point is at a vertex.

structures with small feature sizes, such as short edges and small chamfers. As shown in Fig. 1(b), there is only one source point assigned on the short edge. In this case, it cannot construct the MLS interpolation shape function at the virtual node of interest, because the influence domain should contain at least three source points.

Li and Aluru [15,16] proposed the Hermite-type moving-least-squares (HMLS) interpolation, considering the normal derivative of the unknown in the weighted least-squares minimization approach, when applied to the boundary cloud method (BCM). There is no singular moment matrix for any distribution of interpolation points. The main advantage of the HMLS interpolation shape functions is the use of Cartesian coordinates, meaning the support domain for the weight function can include adjacent edges (see Fig. 2(a)).

However, the interpolation functions are constructed in a linear polynomial basis [15,16]. To improve the accuracy of the HMLS approximation, we use a quadratic polynomial basis. The moment matrix is still singular in some special cases if a complete quadratic basis is used. Furthermore, some scholars [17,18] have pointed out that the stability of the standard MLS approximation declines greatly as the nodes increase. To obtain an accurate algorithm for the HMLS approximation, an improved and incomplete quadratic polynomial basis is proposed.

Following Zhang [12,13], in this paper we present the dual interpolation boundary face method with HMLS approximation (DiBFM-HMLS). The main difference between DiBFM-HMLS and DiBFM-MLS is that HMLS approximation is used, instead of MLS, as the second-layer interpolation. The proposed method inherits the advantages of DiBFM-MLS and is more suitable for structures with small feature sizes. Because the influence domain of a virtual point at a geometric vertex can be extended to other edges (see Fig. 2(b)), there are enough source points to construct relationships with the virtual point. In the proposed method, the HMLS approximation is only used to condense the degrees of freedom for virtual nodes, which is different than in the BCM.

The rest of the paper is outlined as follows: the dual interpolation method with Hermite-type moving-least-squares approximation is described in Section 2. Section 3 introduces the dual interpolation boundary face method with Hermite-type moving-least-squares approximation for potential problems. Numerical results are presented in Section 4 and conclusions are given in Section 5.

2. Dual interpolation method with HMLS approximation

The dual interpolation method includes first-layer and second-layer interpolation. The DiBFM-HMLS and DiBFM-MLS adopt the HMLS and MLS approximation as the second-layer interpolation, respectively. In this section, the second-layer interpolation based on the HMLS approximation is described in detail. Furthermore, an improved and incomplete quadratic polynomial basis is developed to obtain an accurate algorithm of the HMLS approximation.

2.1. First-layer interpolation

The dual interpolation element includes source (s_i) and virtual (v_i) nodes (Fig. 3). For 2-D problems, the potential, u, and normal flux, q, are approximated by first-layer interpolation:

$$u(\xi) = \sum_{\alpha=1}^{n_\alpha} N_\alpha^s(\xi) u(Q_\alpha^s) + \sum_{\beta=1}^{n_\beta} N_\beta^v(\xi) u(Q_\beta^v), \tag{1}$$
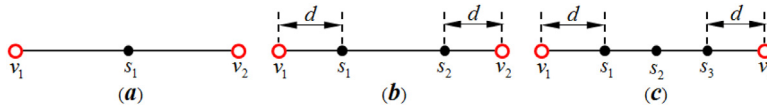
Fig. 3. Dual interpolation elements in 2-D: (a) S1, (b) S2, and (c) S3.

$$q(\xi) = \sum_{\alpha=1}^{n_\alpha} N_\alpha^s(\xi) q(Q_\alpha^s) + \sum_{\beta=1}^{n_\beta} N_\beta^v(\xi) q(Q_\beta^v), \tag{2}$$

where n_α and n_β are the number of source and virtual nodes in the dual interpolation element, $N_\alpha^s(\xi)$, $u(Q_\alpha^s)$, and $q(Q_\alpha^s)$ are the shape function, potential, and normal flux of the αth source node in the dual interpolation element, respectively, and $N_\beta^v(\xi)$, $u(Q_\beta^v)$, and $q(Q_\beta^v)$ are the shape function, potential, and normal flux of the βth virtual node in the dual interpolation element, respectively.

2.2. Second-layer interpolation by HMLS approximation

The HMLS approximation is used to condense the degrees of freedom for all virtual nodes, and can be defined by:

$$u(Q_\beta^v) = \sum_{I=1}^{N_P} \phi_I^{uu}(x^v, y^v) \hat{u}(Q_I^s) + \sum_{I=1}^{N_P} \phi_I^{uq}(x^v, y^v, n^v) \hat{q}(Q_I^s), \tag{3}$$

$$q(Q_\beta^v) = \sum_{I=1}^{N_P} \phi_I^{qu}(x^v, y^v) \hat{u}(Q_I^s) + \sum_{I=1}^{N_P} \phi_I^{qq}(x^v, y^v, n^v) \hat{q}(Q_I^s), \tag{4}$$

where N_p is the number of source nodes located in the influence domain of the virtual node Q_β^v, $\hat{u}(Q_I^s)$ and $\hat{q}(Q_I^s)$ are the fictitious values of the potential and the normal flux at the source node Q_I^s, and (x^v, y^v) and n^v are the Cartesian coordinates and outward normal at the virtual node Q_β^v, respectively. Furthermore, $\phi_I^{uu}(x^v, y^v)$, $\phi_I^{uq}(x^v, y^v, n^v)$, $\phi_I^{qu}(x^v, y^v)$, and $\phi_I^{qq}(x^v, y^v, n^v)$ are the HMLS interpolation shape functions, which are defined by:

$$\phi_I^{uu}(x^v, y^v) = \mathbf{p}^T(x^v, y^v) \mathbf{C}^{-1} \mathbf{p}(x_I^s, y_I^s) w_I(x^v, y^v), \tag{5}$$

$$\phi_I^{uq}(x^v, y^v) = \mathbf{p}^T(x^v, y^v) \mathbf{C}^{-1} \frac{\partial \mathbf{p}}{\partial n}(x_I^s, y_I^s, n_I^s) w_I(x^v, y^v), \tag{6}$$

$$\phi_I^{qu}(x^v, y^v) = \frac{\partial \mathbf{p}^T}{\partial n}(x^v, y^v, n^v) \mathbf{C}^{-1} \mathbf{p}(x_I^s, y_I^s) w_I(x^v, y^v), \tag{7}$$

$$\phi_I^{qq}(x^v, y^v) = \frac{\partial \mathbf{p}^T}{\partial n}(x^v, y^v, n^v) \mathbf{C}^{-1} \frac{\partial \mathbf{p}}{\partial n}(x_I^s, y_I^s, n_I^s) w_I(x^v, y^v), \tag{8}$$

where $\mathbf{p}$ and $\frac{\partial \mathbf{p}}{\partial n}$ are the polynomial basis and its normal derivative, respectively. In [15], $\mathbf{C}$ is defined as the moment matrix and $w_I(x^v, y^v)$ as the weighting function centered at the virtual node Q^v. In our implementation, the Gaussian weighting function is given by:

$$w_I(x^v, y^v) = \begin{cases} \dfrac{e^{-(dx_I/c_x)^2} - e^{-(\bar{d}x/c_x)^2}}{1.0 - e^{-(\bar{d}x/c_x)^2}} \times \dfrac{e^{-(dy_I/c_y)^2} - e^{-(\bar{d}y/c_y)^2}}{1.0 - e^{-(\bar{d}y/c_y)^2}}, & dx_I \leq \bar{d}x \ \text{ and } \ dy_I \leq \bar{d}y \\[4mm] 0, & dx_I > \bar{d}x \ \text{ or } \ dy_I > \bar{d}y \end{cases}, \tag{9}$$

where $dx_I = |x^v - x_I^s|$ and $dy_I = |y^v - y_I^s|$ are the components of distance between Q^v and Q_I^s, c_x and c_y are constants that control the shape of the weighting function, and $\bar{d}x$ and $\bar{d}y$ are sizes of the support domain of Q_I^s.

We propose an improved incomplete quadratic polynomial basis to obtain an accurate algorithm for HMLS approximation. The base interpolating polynomial and its normal derivatives are given by:

$$\mathbf{p}^T(x, y) = \begin{bmatrix} 1 & \tilde{x} & \tilde{y} & \tilde{x}\tilde{y} & \tilde{x}^2 + \tilde{y}^2 \end{bmatrix}, \tag{10}$$

and

$$\frac{\partial \mathbf{p}^T(x, y)}{\partial n} = \begin{bmatrix} 0 & \cos'\alpha & \cos'\beta & \tilde{x}\cos'\beta + \tilde{y}\cos'\alpha & 2\tilde{x}\cos'\alpha + 2\tilde{y}\cos'\beta \end{bmatrix}, \tag{11}$$
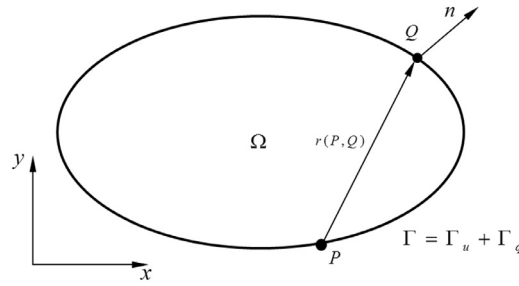
Fig. 4. A 2-D finite domain Ω with boundary Γ.

respectively, in which

$$\tilde{x} = \frac{x - x^e}{h}, \ \tilde{y} = \frac{y - y^e}{h}, \ \cos'\alpha = \frac{\cos\alpha}{h}, \ \text{and} \cos'\beta = \frac{\cos\beta}{h},$$

and

$$h = \max_{1 \le i \le N_P} \min_{1 \le j \le N_P, i \ne j} \left| \mathbf{x}_i^s - \mathbf{x}_j^s \right|,$$

where (x^e, y^e) is the Cartesian coordinate of the fixed point, and α and β are the angles between the outward normal direction and the positive *x*-axis and *y*-axis, respectively. In this paper, we define the coordinate of the virtual node as the fixed point. Recall that the completed quadratic polynomial basis cannot be used because the moment matrix **C** becomes singular when all the source nodes lie along either $\tilde{x} = 0$ or $\tilde{y} = 0$ (see Appendix A for details).

3. DiBFM with HMLS approximation for solving potential problems

3.1. Boundary integral equation

The potential problem governed by Laplace's equation with boundary conditions is given by:

$$\begin{aligned} \nabla^2 u &= 0, \forall \mathbf{x} \in \Omega \\ u &= \bar{u}, \forall \mathbf{x} \in \Gamma_u \\ q &= \frac{\partial u}{\partial n} = \bar{q}, \forall \mathbf{x} \in \Gamma_q, \end{aligned} \tag{12}$$

where the domain Ω is enclosed by the boundary $\Gamma = \Gamma_u + \Gamma_q$, $\bar{u}$ and $\bar{q}$ are the prescribed values of the potential and the normal flux on the boundaries Γ_u and Γ_q, respectively, and *n* is the outward normal of the boundary Γ(see Fig. 4).

This problem can be also evaluated using a boundary integral equation (BIE) [19]:

$$c(P)u(P) = \int_\Gamma u^*(P, Q)q(Q)d\Gamma(Q) - \int_\Gamma q^*(P, Q)u(Q)d\Gamma(Q), \tag{13}$$

where *P* is the source point, *Q* is the field point, $c(P) = 1/2$ when *P* is on the smooth boundary, and $u^*(P, Q)$ and $q^*(P, Q)$ are fundamental solutions. For 2-D potential problems, $u^*(P, Q)$ and $q^*(P, Q)$ are given by:

$$u^*(P, Q) = \frac{1}{2\pi} \ln\left(\frac{1}{r(P, Q)}\right), \tag{14}$$

$$q^*(P, Q) = \frac{\partial u^*(P, Q)}{\partial n(Q)}, \tag{15}$$

where $r(P, Q)$ is the Euclidean distance between points *P* and *Q*.

3.2. Discretization of the BIE

The numbers of elements, source nodes, virtual nodes, and field nodes are denoted *NE, NS, NV*, and *NM*, respectively. As mentioned earlier, the boundary integral equations are only collocated at the source nodes. Thus, the discretized form of Eq. (13) can be written as:

$$\sum_{j=1}^{NE} \sum_{\alpha=1}^{M^j} h_{ij}^\alpha u_j^\alpha = \sum_{j=1}^{NE} \sum_{\alpha=1}^{M^j} g_{ij}^\alpha q_j^\alpha, i = 1, 2, \dots, NS, \tag{16}$$

with

$$h_{ij}^{\alpha} = \int_{\Gamma_j} q^*(P_i, Q) N_j^{\alpha}(Q) d\Gamma(Q) + \frac{1}{2}\delta_{ij}^{\alpha}, \tag{17}$$

$$g_{ij}^{\alpha} = \int_{\Gamma_j} u^*(P_i, Q) N_j^{\alpha}(Q) d\Gamma(Q), \tag{18}$$

and

$$\delta_{ij}^{\alpha} = \begin{cases} 1, \text{ if the } i^{\text{th}} \text{ source node is the } \alpha^{\text{th}} \text{ source node in the } j^{\text{th}} \text{ element} \\ 0 \end{cases}, \tag{19}$$

where u_j^{α} and q_j^{α} are the potential and the normal flux of the αth interpolation node of the jth element, respectively, M^j denotes the number of interpolation nodes of the jth element, and $N_j^{\alpha}(Q)$ represents the shape function of the first-layer interpolation for the αth interpolation node of the jth element. The matrix form of Eq. (16) is:

$$\mathbf{Hu} = \mathbf{Gq}, \tag{20}$$

where $\mathbf{H}$ and $\mathbf{G}$ are $NS \times NM$ coefficient matrices, and $\mathbf{u}$ and $\mathbf{q}$ are $NM \times 1$ vectors containing the potentials and the normal fluxes of all field nodes, respectively. The coefficient matrices are not square because the BIEs are not collocated at virtual nodes. Our method using HMLS approximation condenses the degrees of freedom relating to all virtual nodes.

3.3. Condensation of degrees of freedom for virtual nodes when using HMLS approximation

Differentiating the source and virtual nodes in Eq. (20), we obtain:

$$\begin{bmatrix} \mathbf{H}^{ss} & \mathbf{H}^{sv} \end{bmatrix} \begin{Bmatrix} \mathbf{u}^s \\ \mathbf{u}^v \end{Bmatrix} = \begin{bmatrix} \mathbf{G}^{ss} & \mathbf{G}^{sv} \end{bmatrix} \begin{Bmatrix} \mathbf{q}^s \\ \mathbf{q}^v \end{Bmatrix}, \tag{21}$$

where $\mathbf{u}^s$ and $\mathbf{q}^s$ are the $NS \times 1$ potential and normal flux vectors for the source nodes, $\mathbf{u}^v$ and $\mathbf{q}^v$ are the $NV \times 1$ vectors corresponding to the virtual nodes, and $\mathbf{H}^{ss}$, $\mathbf{G}^{ss}$, $\mathbf{H}^{sv}$, and $\mathbf{G}^{sv}$ are the $NS \times NS$, $NS \times NS$, $NS \times NV$, $NS \times NV$ coefficient matrices corresponding to the vectors $\mathbf{u}^s$, $\mathbf{q}^s$, $\mathbf{u}^v$, and $\mathbf{q}^v$, respectively.

The vectors $\mathbf{u}^v$ and $\mathbf{q}^v$ contain both known and unknown variables, and can be written in the following form:

$$\mathbf{u}^v = \bar{\mathbf{u}}^v + \widehat{\mathbf{u}}^v, \tag{22}$$

$$\mathbf{q}^v = \bar{\mathbf{q}}^v + \widehat{\mathbf{q}}^v, \tag{23}$$

where $\bar{\mathbf{u}}^v$, $\widehat{\mathbf{u}}^v$, $\bar{\mathbf{q}}^v$, and $\widehat{\mathbf{q}}^v$ are the $NV \times 1$ vectors describing the known and unknown potentials and normal fluxes of the virtual nodes, respectively.

Each unknown potential and normal flux in $\widehat{\mathbf{u}}^v$ and $\widehat{\mathbf{q}}^v$ can be approximated using HMLS approximation defined by Eqs. (3) and (4). As a result, $\widehat{\mathbf{u}}^v$ and $\widehat{\mathbf{q}}^v$ can be expressed as follows:

$$\widehat{\mathbf{u}}^v = \mathbf{\Phi}_{uu}^{vs}\mathbf{u}^s + \mathbf{\Phi}_{uq}^{vs}\mathbf{q}^s, \tag{24}$$

$$\widehat{\mathbf{q}}^v = \mathbf{\Phi}_{qu}^{vs}\mathbf{u}^s + \mathbf{\Phi}_{qq}^{vs}\mathbf{q}^s, \tag{25}$$

where $\mathbf{\Phi}_{uu}^{vs}$, $\mathbf{\Phi}_{uq}^{vs}$, $\mathbf{\Phi}_{qu}^{vs}$, and $\mathbf{\Phi}_{qq}^{vs}$ are shape function matrices obtained by the HMLS approximation (Section 2.2).

Combining Eqs. (21), (24), and (25), we can obtain:

$$\mathbf{H}^{ss}\mathbf{u}^s + \mathbf{H}^{sv}\mathbf{\Phi}_{uu}^{vs}\mathbf{u}^s + \mathbf{H}^{sv}\mathbf{\Phi}_{uq}^{vs}\mathbf{q}^s + \mathbf{H}^{sv}\bar{\mathbf{u}}^v = \mathbf{G}^{ss}\mathbf{q}^s + \mathbf{G}^{sv}\mathbf{\Phi}_{qu}^{vs}\mathbf{u}^s + \mathbf{G}^{sv}\mathbf{\Phi}_{qq}^{vs}\mathbf{q}^s + \mathbf{G}^{sv}\bar{\mathbf{q}}^v, \tag{26}$$

and then with sorting order and combining the similar items, we obtain:

$$\mathbf{H}^s\mathbf{u}^s = \mathbf{G}^s\mathbf{q}^s + \mathbf{b}^v, \tag{27}$$

with

$$\mathbf{H}^s = \mathbf{H}^{ss} + \mathbf{H}^{sv}\mathbf{\Phi}_{uu}^{vs} - \mathbf{G}^{sv}\mathbf{\Phi}_{qu}^{vs}, \tag{28}$$

$$\mathbf{G}^s = \mathbf{G}^{ss} + \mathbf{G}^{sv}\mathbf{\Phi}_{qq}^{vs} - \mathbf{H}^{sv}\mathbf{\Phi}_{uq}^{vs}, \tag{29}$$

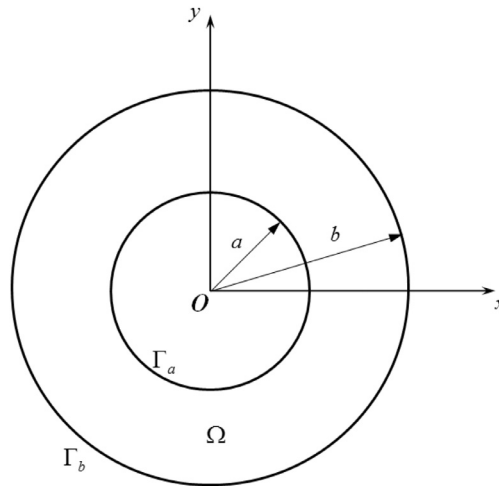$$\mathbf{b}^v = -\mathbf{H}^{sv}\bar{\mathbf{u}}^v + \mathbf{G}^{sv}\bar{\mathbf{q}}^v. \tag{30}$$

Fig. 5. A potential problem of an annular region Ω.

Applying the boundary conditions to Eq. (27) results in the following:

$$\left\{ \bar{\mathbf{H}}^s \quad \widehat{\mathbf{H}}^s \right\} \left\{ \begin{array}{c} \bar{\mathbf{u}}^s \\ \widehat{\mathbf{u}}^s \end{array} \right\} = \left\{ \bar{\mathbf{G}}^s \quad \widehat{\mathbf{G}}^s \right\} \left\{ \begin{array}{c} \bar{\mathbf{q}}^s \\ \widehat{\mathbf{q}}^s \end{array} \right\} + \mathbf{b}^v, \tag{31}$$

where $\bar{\mathbf{u}}^s$, $\widehat{\mathbf{u}}^s$, $\bar{\mathbf{q}}^s$, and $\widehat{\mathbf{q}}^s$ are the known and unknown potentials and normal flux vectors for the source nodes, and $\bar{\mathbf{H}}^s$, $\widehat{\mathbf{H}}^s$, $\bar{\mathbf{G}}^s$, and $\widehat{\mathbf{G}}^s$ are the coefficient matrices corresponding to the vectors $\bar{\mathbf{u}}^s$, $\widehat{\mathbf{u}}^s$, $\bar{\mathbf{q}}^s$, and $\widehat{\mathbf{q}}^s$, respectively.

Finally, Eq. (31) describes a system of linear equations:

$$\mathbf{Ax} = \mathbf{b}, \tag{32}$$

in which

$$\mathbf{A} = \left\{ \widehat{\mathbf{H}}^s \quad \widehat{\mathbf{G}}^s \right\}, \ \mathbf{x} = \left\{ \begin{array}{c} \widehat{\mathbf{u}}^s \\ \widehat{\mathbf{q}}^s \end{array} \right\}, \ \mathbf{b} = \bar{\mathbf{G}}^s \bar{\mathbf{q}}^s + \mathbf{b}^v - \bar{\mathbf{H}}^s \bar{\mathbf{u}}^s,$$

where $\mathbf{A}$ is a $NS \times NS$ coefficient matrix, $\mathbf{x}$ is a $NS \times 1$ boundary vector of unknowns only for the source nodes, and $\mathbf{b}$ is a $NS \times 1$ known vector.

The size of Eq. (32) is identical to that in the traditional BEM with discontinuous elements, while the DiBFM-HMLS can achieve higher accuracy by improving the interpolation of boundary elements.

4. Numerical examples

We present five numerical examples to demonstrate the benefits of the proposed method for solving Laplace's equation. The first example demonstrates the accuracy and efficiency of the presented method. The second and third examples highlight the advantages of our method to solve for structures having small feature sizes. The fourth example demonstrates its ability to handle complex geometry, and the fifth is a real-world example that attests to the practicability of the proposed method.

Error estimation and convergence of the presented method are measured by the relative error, defined as:

$$error = \frac{1}{\left| v^{(e)} \right|_{\max}} \sqrt{\frac{1}{M} \sum_{i=1}^{M} \left[v_i^{(e)} - v_i^{(n)} \right]^2}, \tag{33}$$

where $|v^{(e)}|_{\max}$ is the maximum value of the exact potential solution u or normal flux q over M sample points, and superscripts e and n denote the exact and computed solutions, respectively. In all numerical examples, the offset parameter d in the dual interpolation element is chosen as 0.25 and $\bar{d}x/c_x = \bar{d}y/c_y = 3$ [Eq. (9)]. Err_u and Err_q denote the relative errors for u and q, respectively.

4.1. Annular region

The first example is a potential problem of an annular region [20] (e.g., heat conduction) depicted in Fig. 5. The potential and normal flux boundary conditions are specified along the inner and outer boundaries, Γ_a and Γ_b, respectively. The

Table 1
Relative errors of the results from each method.

DiBFM-HMLS					Traditional BEM			
NS	u_b	q_a	Err_u_b	Err_q_a	u_b	q_a	Err_u_b	Err_q_a
36	377.265895	−399.989868	1.86E−05	2.53E−05	376.723612	−401.771546	1.419E−03	4.43E−03
72	377.262389	−399.994926	9.32E−06	1.27E−05	377.140972	−400.400662	3.125E−04	1.00E−03
360	377.259576	−399.998985	1.87E−06	2.54E−06	377.254783	−400.014803	1.084E−05	3.70E−05
720	377.259224	−399.999492	9.33E−07	1.27E−06	377.257873	−400.003629	2.649E−06	9.07E−06
1440	377.259048	−399.999746	4.66E−07	6.35E−07	377.258622	−400.000533	6.633E−07	1.33E−06
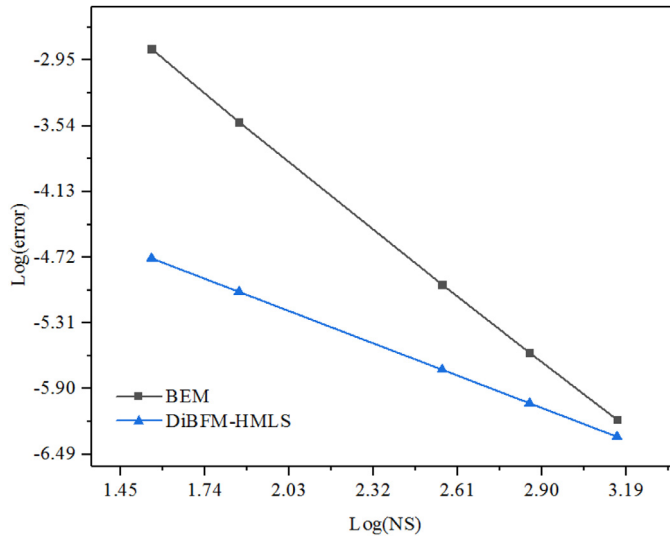
Fig. 6. Comparison of convergence for u_b.

analytical solution to this problem is given by:

$$u(r) = u_a + q_b b \ln\left(\frac{r}{a}\right), \tag{34}$$

where u_a and q_b are the values of u and q on boundaries Γ_a and Γ_b, respectively, and r is the radial coordinate in polar coordinates centered on O. This gives the exact values of $u_b = u(b) = u_a + q_b b \ln(\frac{b}{a})$ and $q_a = \frac{\partial u}{\partial n}(a) = -q_b \frac{b}{a}$. We chose $a = 1$, $b = 2$, $u_a = 100.0$, and $q_b = 200.0$, giving $u_b = 377.258872$ and $q_a = $ -400.0.

This example is presented to demonstrate the accuracy of DiBFM-HMLS in comparison with results obtained by Liu and Nishimura [20] using the traditional BEM. The physical variables on the boundaries are approximated by S1 elements in DiBFM-HMLS. The values of u_b, q_a, and corresponding relative errors are listed in Table 1. The relative errors for u_b and q_a are plotted in Figs. 6 and 7.

Using the same number of source points, DiBFM-HMLS yields higher accuracy and converges faster to the exact solution than the traditional BEM, because the integrand quantities in DiBFM-HMLS are calculated directly from the curves rather than from elements [8,9].

4.2. Slender structure with short edges

Our second example is the potential problem of a needlelike structure (Fig. 8) with a cubic polynomial solution for u. The Dirichlet boundary conditions are specified along the three short edges DO, AB, and BC, given by:

$$u = x^3 + 3y^3 - 9x^2y - 3xy^2 + y. \tag{35}$$

Neumann boundary conditions are specified for the two long edges CD and OA, given by:

$$q = \frac{\partial u}{\partial n} = \begin{cases} 9y^2 - 9x^2 - 6xy + 1 & \text{for } y = 0.5, \\ 9x^2 - 9y^2 + 6xy - 1 & \text{for } y = -0.5. \end{cases} \tag{36}$$

The exact solution for u is given by:

$$u = x^3 + 3y^3 - 9x^2y - 3xy^2 + y, \tag{37}$$

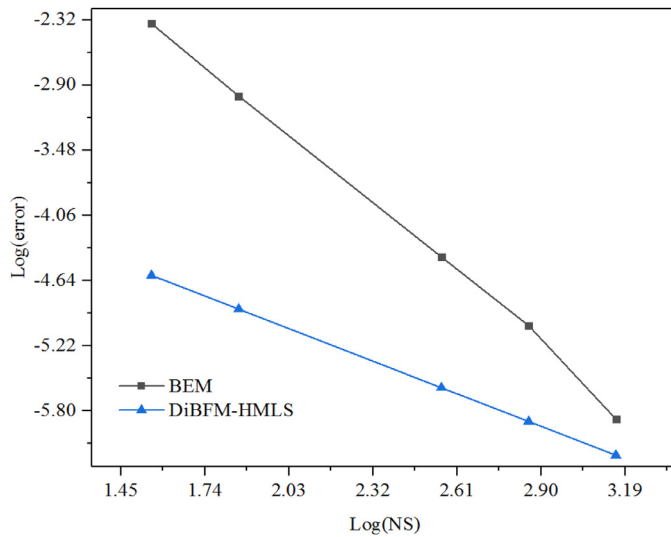which satisfies Laplace's equation with the above boundary conditions.

Fig. 7. Comparison of convergence for q_a.
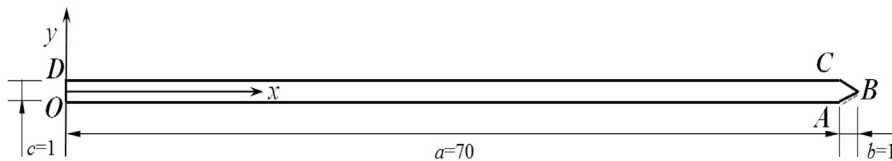

Fig. 8. A potential problem of a slender structure with short edges.

Table 2
Relative errors and CPU time for each method.

DiBFM-HMLS				DiBFM-MLS			BEM		
NS	Err_u	Err_q	Time (s)	Err_u	Err_q	Time (s)	Err_u	Err_q	Time (s)
23	1.24E−03	2.52E−03	0.221	3.05E−03	5.37E−03	0.213	8.44E−02	6.39E−02	0.186
43	6.65E−05	5.91E−04	0.382	3.06E−04	5.26E−03	0.382	4.38E−02	5.53E−02	0.311
83	8.98E−06	2.25E−04	0.792	6.30E−05	5.26E−03	0.763	1.96E−02	5.24E−02	0.628
163	2.31E−06	1.22E−04	1.809	5.28E−05	5.25E−03	1.595	8.53E−03	5.14E−02	1.353
323	1.14E−06	7.41E−05	3.745	5.51E−05	5.25E−03	3.612	4.56E−03	5.09E−02	2.784

This example demonstrates the advantages of the proposed method when solving for a slender structure with small feature sizes, which is difficult using the DiBFM-MLS. The boundary unknowns on all edges are approximated by constant elements with different methods. It is worth noting that only one constant element is allocated on each of the short edges *DO, AB*, and *BC*.

Table 2 lists the relative errors and CPU time with increasing numbers of source points on the long edges. The CPU time is mainly spent in calculating boundary integrals, constructing the second-layer interpolation, and solving the final system of linear equations. The relative errors for the boundary unknowns *u* and *q* are also plotted in Figs. 9 and 10, respectively. Numerical and exact results of the normal flux *q*, along the line *AB* with 323 source nodes, are plotted in Fig. 11.

Between Figs. 9 and 12, the accuracy of BEM and DiBFM-MLS for *q* scarcely changes with increasing number of source points on the long edge. However, accuracy is substantially improved for DiBFM-HMLS. For DiBFM-MLS, the element on the short edges is a traditional constant element rather than a S1 dual interpolation element, because it cannot construct the MLS interpolation shape function on short edges where only one source point is distributed. As a result, the solutions for *q* using DiBFM-MLS are poor, as with the conventional BEM. This problem is solved in DiBFM-HMLS by searching for the source points located on adjacent long edges (e.g., edges *OA* and *CD*). These results demonstrate that our method is more effective at solving for a slender structure with small feature sizes than the other two numerical methods.

4.3. Multi-groove thin-wall structure

We consider a Dirichlet problem of a multi-groove thin-wall structure with a cubic polynomial solution for *u*. The dimensions of the structure are given in Fig. 13. The potential boundary conditions are imposed on all edges corresponding to
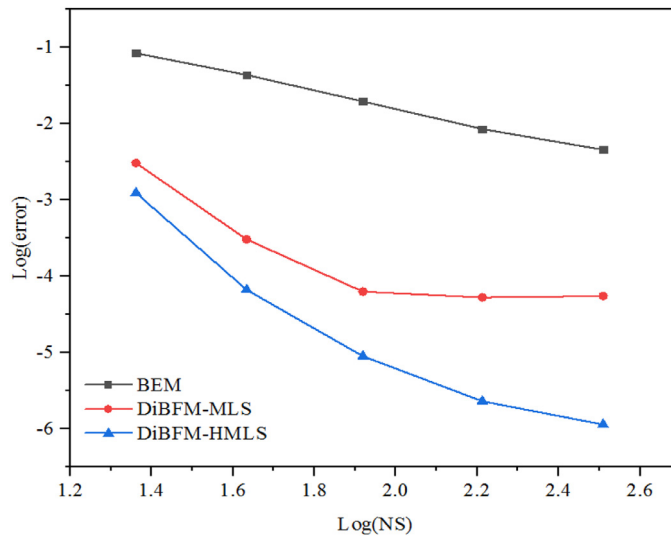
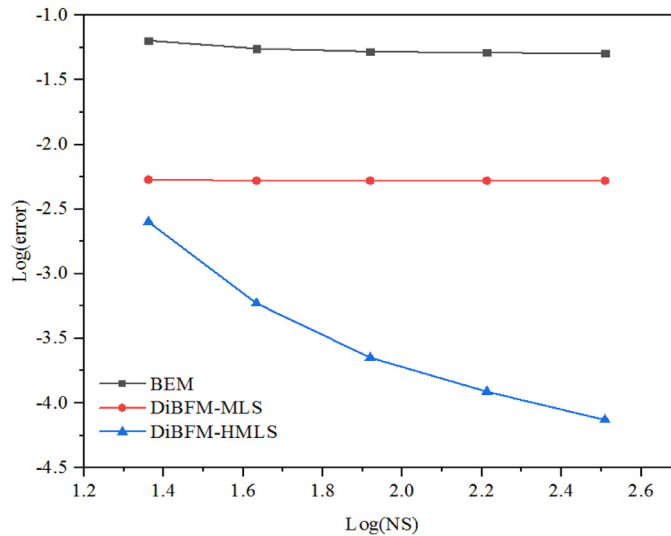**Fig. 9.** Comparison of relative errors for *u*.

Fig. 10. Comparison of relative errors for *q*.

the following exact solution:

$$u = -x^3 - y^3 + 3x^2y + 3xy^2 + 2x - 2y. \tag{38}$$

Thus, the solution for *u* satisfies Laplace's equation with the corresponding boundary conditions.

This example is given to demonstrate the ability of DiBFM-HMLS in solving for a thin-wall structure with multiple short edges. The field variables on the long edges are approximated by constant elements with different methods and only one constant element is distributed on the short edge (of length *d*). The relative errors for the normal fluxes *q* with increasing number of source points on long edges are listed in Table 3 and plotted in Fig. 14, respectively. The numerical results of normal fluxes *q* compared with the exact solution, along the curve *mn* obtained using 565 source nodes, are shown in Fig. 15, in which the abscissa is the number of sample nodes along the curve *mn*.

Table 3 and Fig. 16 show that the accuracy and efficiency of our proposed method are better than that of the DiBFM-MLS and conventional BEM. Similarly, the results cannot be improved with increasing source points in the latter two methods, for the same reason as in the previous example (Section 4.2). The comparison demonstrates that our method can approximate the physical fields around the short edges accurately when using only one source point.
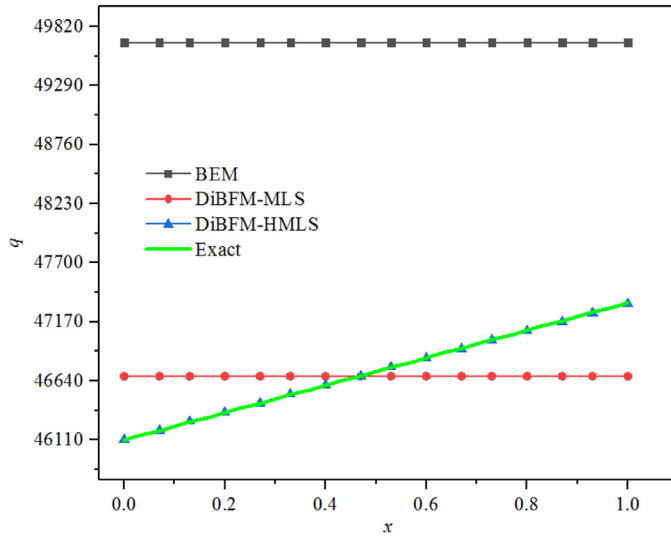
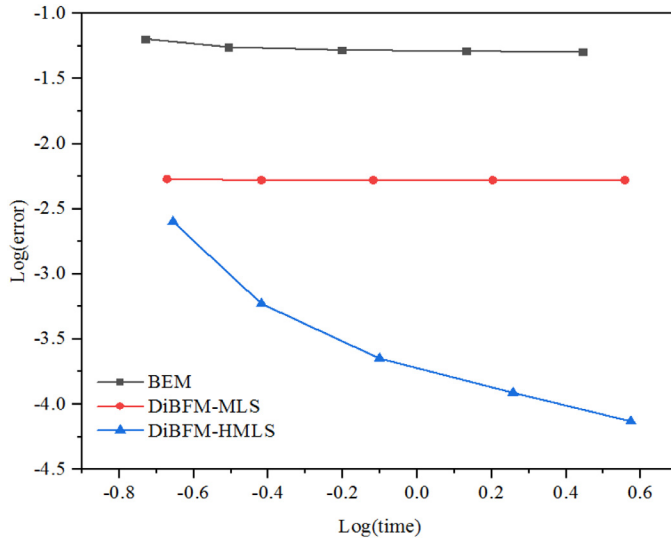**Fig. 11.** Comparison of accuracy for q along line AB.

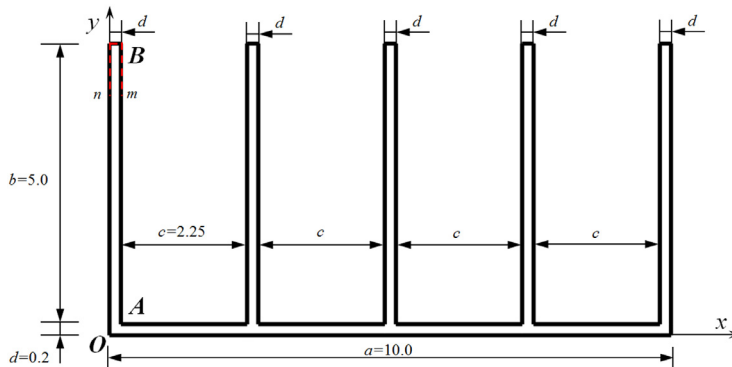**Fig. 12.** Comparison of computational efficiency for q.

Fig. 13. A Dirichlet problem of a multi-groove thin-wall structure.

Table 3
Relative errors and CPU time of the results with different methods.

DiBFM-HMLS			DiBFM-MLS		BEM	
NS	Err_q	Time (s)	Err_q	Time (s)	Err_q	Time (s)
77	3.86E−03	1.099	1.68E−03	1.099	1.87E−01	0.87
145	1.33E−03	2.331	1.68E−03	2.218	8.19E−02	1.760
285	3.49E−04	4.591	1.68E−03	4.440	3.06E−02	3.629
425	1.65E−04	7.469	1.70E−03	7.117	1.66E−02	5.586
565	9.20E−05	10.339	1.72E−03	9.744	1.34E−02	7.463
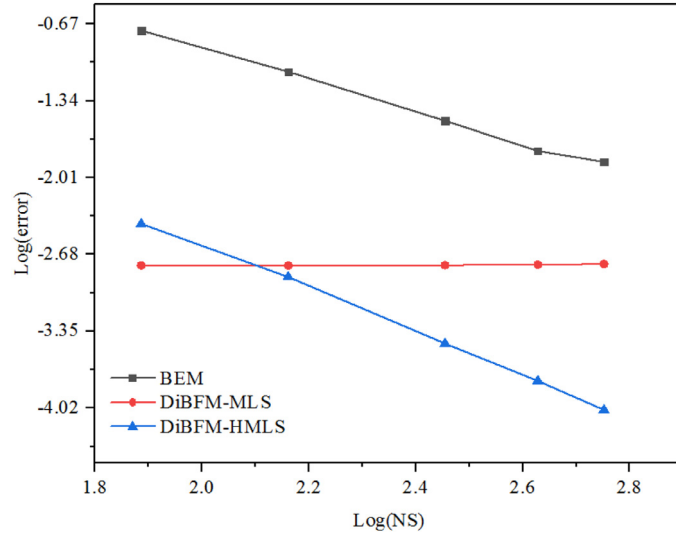
Fig. 14. Comparison of relative errors for q.
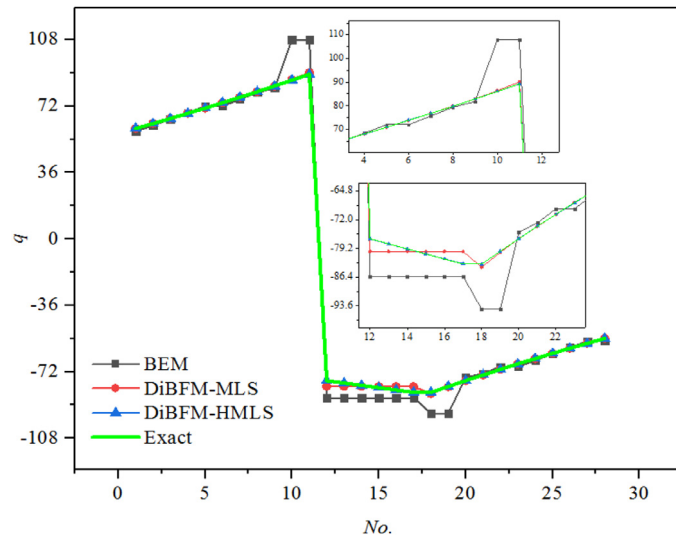
Fig. 15. Comparison of accuracy for q along the curve mn.

4.4. Wheel structure

To demonstrate the ability of our method to handle arbitrary complex geometries, we analyze a Dirichlet problem of a wheel structure. The dimensions and imposed Dirichlet boundary conditions are shown in Fig. 17(a) and (b), respectively. For this problem, we chose $r_1 = 5.0$, $r_2 = 50.0$, and $r_3 = 65.0$. The prescribed u along all boundary edges are chosen as
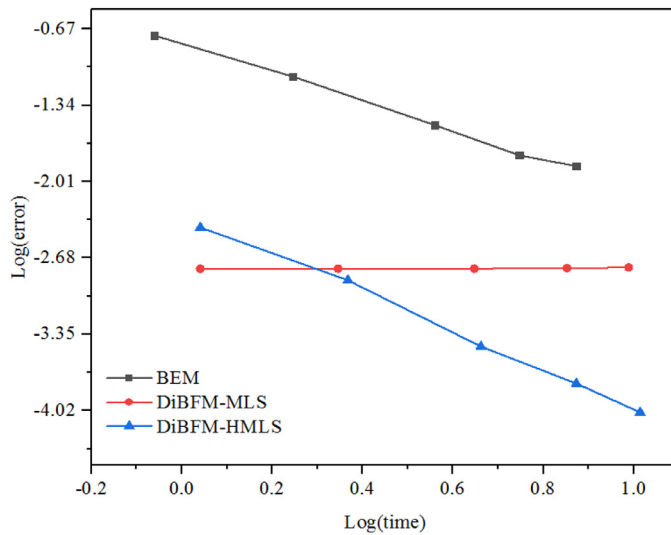
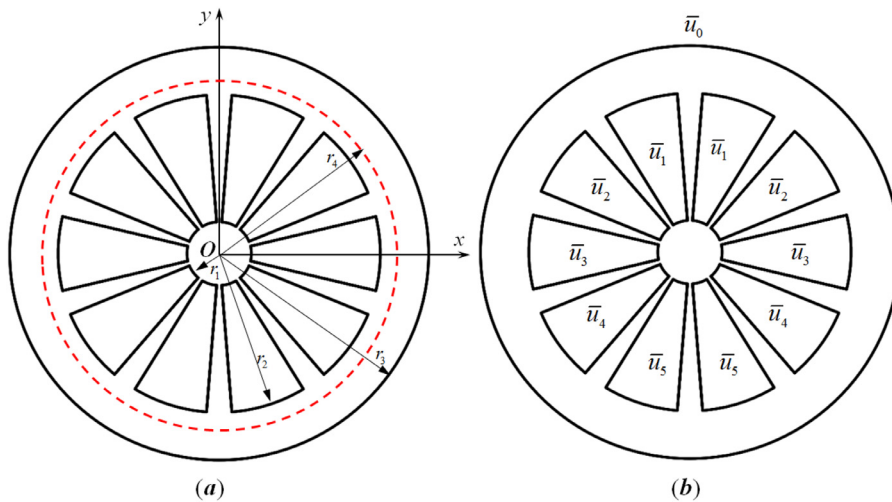**Fig. 16.** Comparison of computational efficiency for q.

Fig. 17. Dirichlet problem of a wheel structure: (a) geometric model and (b) boundary conditions for all edges.

$\bar{u}_0 = 80.0$, $\bar{u}_1 = 10.0$, $\bar{u}_2 = 20.0$, $\bar{u}_3 = 30.0$, $\bar{u}_4 = 40.0$, and $\bar{u}_5 = 50.0$. The physical variables are approximated with quadratic elements.

The Fig. 18 presents the comparisons of the potential along the red dotted curve in Fig. 17, for $r_4 = 54.0$, between different methods. The labels "426_nSrc" and "603_nSrc" refer to the use of 426 and 603 source points, respectively. The numerical results of FEM with 797767 nodes are used as reference solutions. Furthermore, Fig. 19 shows the potential distribution in the whole domain.

As shown in Fig. 18, the numerical results of potential obtained by DiBFM-MLS, DiBFM-HMLS, and the reference solution are indistinguishable. The contour plots of potential in Fig. 19 are almost the same. Therefore, this numerical example demonstrates that a high level of accuracy can be obtained by DiBFM-HMLS even when applied to complex geometries, and that DiBFM-HMLS inherits the advantages of DiBFM-MLS.

4.5. Steady heat conduction problem of a casting mold

We consider the steady heat conduction problem of a casting mold filled with molten aluminum. We chose a coefficient of heat conduction for the casting mold of $k = 7.2$ W/(m•K)). The dimensions of the structure and boundary conditions are shown in Fig. 20(a) and (b), respectively. The temperature of the inner faces Γ_u of the casting mold is 660°C, which is the
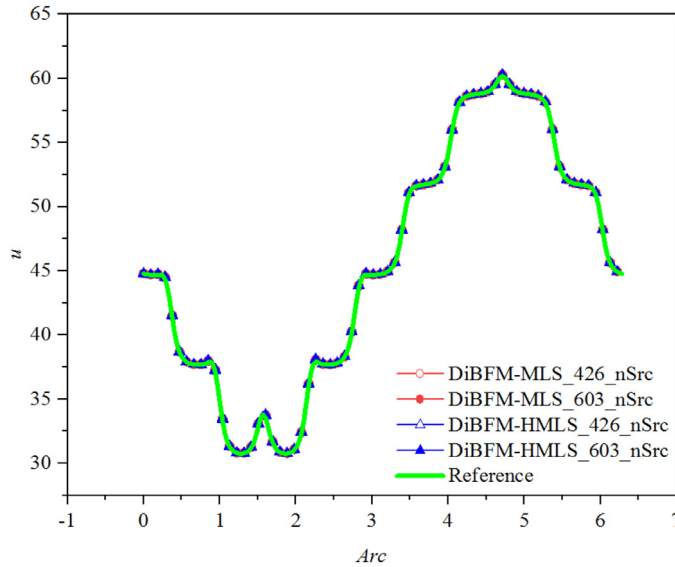
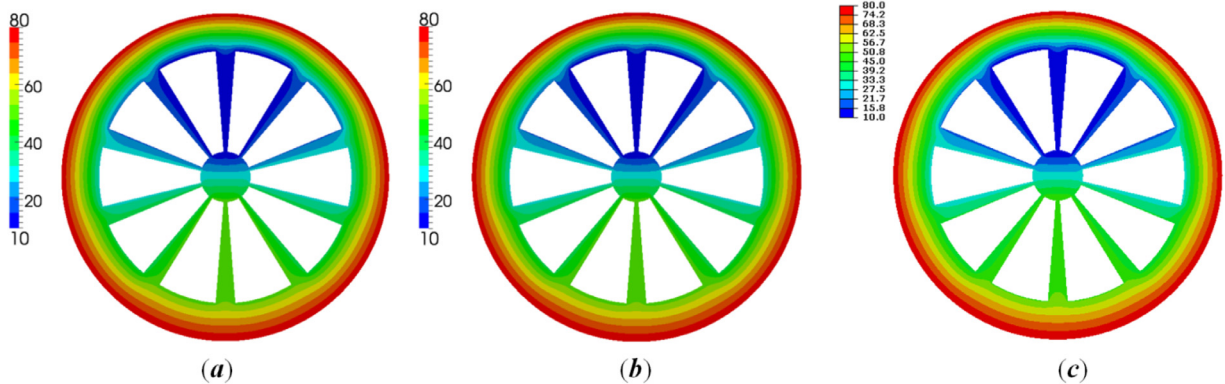**Fig. 18.** The potential along the red dotted line.

Fig. 19. Contour plots of potential: (a) DiBFM-HMLS with 603 source points, (b) DiBFM-MLS with 603 source points, and (c) FEM with 797,767 nodes.

melting point of aluminum. The outside faces Γ_r of the casting mold are exposed to the air. Thus, the convection boundary conditions (i.e., Robin boundary conditions) are considered as follows:

$$q = h(u - u_b) \tag{39}$$

where q and u are the heat flux and temperature on the outside faces, respectively, h is the convection coefficient, and u_b is the ambient temperature. We chose $h = 0.8$ and $u_b = 23°$C.

Again, the physical variables are approximated with quadratic elements. The results of temperature u along the red line MN in Fig. 20(b) obtained by DiBFM-HMLS, DiBFM-MLS, and FEM are shown in Fig. 21. Fig. 22 shows the temperature distribution in the whole domain. The numerical results of FEM with 327,951 nodes are taken as the reference solutions. The labels "213_nSrc" and "735_nSrc" refer to the use of 213 and 735 source points, respectively. Note that only one element is allocated on the short edges when the number of source points is 213. As shown in Fig. 21, the results obtained by DiBFM-MLS with 213 source points are inaccurate, while the results from DiBFM-HMLS with the same number of source points are accurate. Both Fig. 21 and Fig. 22 show that the numerical results obtained by DiBFM-HMLS with few source nodes are the same as the reference solution. Therefore, this numerical example demonstrates the practicability of our method when applied to a real-world problem.

5. Discussion and conclusions

We have enhanced the DiBFM with HMLS approximation instead of the standard MLS approximation. The DiBFM-HMLS inherits the advantages of DiBFM-MLS, achieving higher accuracy and faster convergence rates than those for a traditional BEM. The second-layer interpolation in the proposed method is the HMLS approximation, which is performed directly in
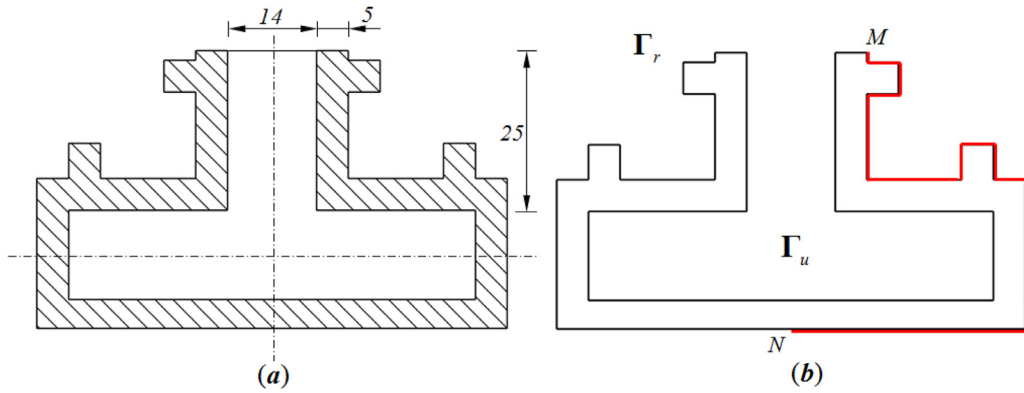
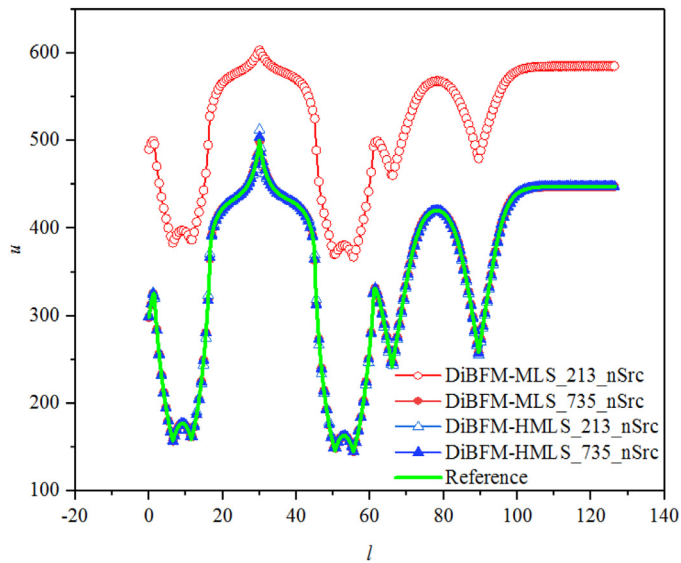**Fig. 20.** Steady heat conduction problem of a casting mold: (a) geometric model and (b) boundary conditions.

Fig. 21. The temperature along the red line.
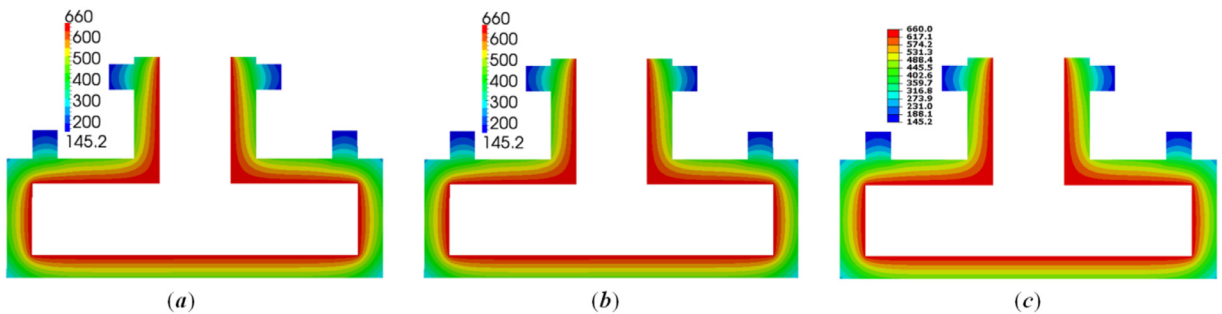

Fig. 22. Contour plots of temperature: (a) DiBFM-HMLS with 735 source points, (b) DiBFM-MLS with 735 source points, and (c) FEM with 327,951 nodes.

Cartesian coordinates rather than the cyclic coordinates of curves. When compared with the DiBFM-MLS, the proposed method has two merits. First, the proposed method can easily solve for structures with small feature sizes, because the influence domain of any virtual node can be extended to the other adjacent edges. Second, it eliminates the difficulties in obtaining the parametric equation for complex curves. Furthermore, an improved and incomplete quadratic polynomial basis is presented to obtain an accurate algorithm for HMLS approximation. All presented numerical examples illustrate the accuracy and efficiency of our method when solving for various geometries with different types of boundary condition.

In this study, we used an improved and incomplete quadratic polynomial basis in the HMLS approximation. In future work, we plan to develop a complete quadratic or higher order polynomial basis. We also plan to extend the range of applicability of the method to the 3-D case.

Acknowledgments

Appendix A. Definition of the moment matrix in complete quadratic polynomial basis

The complete quadratic polynomial basis and its normal derivatives are given by:

$$\mathbf{p}^{\mathrm{T}}(x, y) = \begin{bmatrix} 1 & \tilde{x} & \tilde{y} & \tilde{x}^2 & \tilde{x}\tilde{y} & \tilde{y}^2 \end{bmatrix}, \tag{40}$$

and

$$\frac{\partial \mathbf{p}^{\mathrm{T}}(x, y)}{\partial n} = \begin{bmatrix} 0 & \cos'\alpha & \cos'\beta & 2\tilde{x}\cos'\alpha & \tilde{x}\cos'\beta + \tilde{y}\cos'\alpha & 2\tilde{y}\cos'\beta \end{bmatrix}, \tag{41}$$

and the moment matrix $\mathbf{C}_t$ is defined in [15] as follows:

$$\mathbf{C_t} = \sum_{I}^{NP} w_I \begin{bmatrix} 1 & \tilde{x}_I & \tilde{y}_I & \tilde{x}_I^2 & \tilde{x}_I\tilde{y}_I & \tilde{y}_I^2 \\ \tilde{x}_I & \tilde{x}_I^2 & \tilde{x}_I\tilde{y}_I & \tilde{x}_I^3 & \tilde{x}_I^2\tilde{y}_I & \tilde{x}_I\tilde{y}_I^2 \\ \tilde{y}_I & \tilde{x}_I\tilde{y}_I & \tilde{y}_I^2 & \tilde{x}_I^2\tilde{y}_I & \tilde{x}_I\tilde{y}_I^2 & \tilde{y}_I^3 \\ \tilde{x}_I^2 & \tilde{x}_I^3 & \tilde{x}_I^2\tilde{y}_I & \tilde{x}_I^4 & \tilde{x}_I^3\tilde{y}_I & \tilde{x}_I^2\tilde{y}_I^2 \\ \tilde{x}_I\tilde{y}_I & \tilde{x}_I^2\tilde{y}_I & \tilde{x}_I\tilde{y}_I^2 & \tilde{x}_I^3\tilde{y}_I & \tilde{x}_I^2\tilde{y}_I^2 & \tilde{x}_I\tilde{y}_I^3 \\ \tilde{y}_I^2 & \tilde{x}_I\tilde{y}_I^2 & \tilde{y}_I^3 & \tilde{x}_I^2\tilde{y}_I^2 & \tilde{x}_I\tilde{y}_I^3 & \tilde{y}_I^4 \end{bmatrix}$$

$$+ \sum_{I}^{n} w_I \begin{bmatrix} 0 & 0 & 0 & 0 & 0 & 0 \\ 0 & (\cos'\alpha_I)^2 & \cos'\alpha_I\cos'\beta_I & 2\tilde{x}_I(\cos'\alpha_I)^2 & \cos'\alpha_I\frac{\partial(\tilde{x}_I\tilde{y}_I)}{\partial n_I} & 2\tilde{y}_I\cos'\beta_I\cos'\alpha_I \\ 0 & \cos'\alpha_I\cos'\beta_I & (\cos'\beta_I)^2 & 2\tilde{x}_I\cos'\alpha_I\cos'\beta_I & \cos'\beta_I\frac{\partial(\tilde{x}_I\tilde{y}_I)}{\partial n_I} & 2\tilde{y}_I(\cos'\beta_I)^2 \\ 0 & 2\tilde{x}_I(\cos'\alpha_I)^2 & 2\tilde{x}_I\cos'\alpha_I\cos'\beta_I & 4\tilde{x}_I^2(\cos'\alpha_I)^2 & 2\tilde{x}_I\cos'\alpha_I\frac{\partial(\tilde{x}_I\tilde{y}_I)}{\partial n_I} & 4\tilde{x}_I\tilde{y}_I\cos'\alpha_I\cos'\beta_I \\ 0 & \cos'\alpha_I\frac{\partial(\tilde{x}_I\tilde{y}_I)}{\partial n_I} & \cos'\beta_I\frac{\partial(\tilde{x}_I\tilde{y}_I)}{\partial n_I} & 2\tilde{x}_I\cos'\alpha_I\frac{\partial(\tilde{x}_I\tilde{y}_I)}{\partial n_I} & \left(\frac{\partial(\tilde{x}_I\tilde{y}_I)}{\partial n_I}\right)^2 & 2\tilde{y}_I\cos'\beta_I\frac{\partial(\tilde{x}_I\tilde{y}_I)}{\partial n_I} \\ 0 & 2\tilde{y}_I\cos'\alpha_I\cos'\beta_I & 2\tilde{y}_I(\cos'\beta_I)^2 & 4\tilde{x}_I\tilde{y}_I\cos'\alpha_I\cos'\beta_I & 2\tilde{y}_I\cos'\beta_I\frac{\partial(\tilde{x}_I\tilde{y}_I)}{\partial n_I} & 4\tilde{y}_I^2(\cos'\beta_I)^2 \end{bmatrix} \tag{42}$$

with

$$\frac{\partial(\tilde{x}_I\tilde{y}_I)}{\partial n_I} = \tilde{x}_I\cos'\beta_I + \tilde{y}_I\cos'\alpha_I. \tag{43}$$

As shown in Eqs (42) and (43), if all the interpolation points are located on the straight line $\tilde{x} = 0$ (or $\tilde{y} = 0$), i.e. $\tilde{x}_I = 0$ (or $\tilde{y}_I = 0$) and $\cos'\beta_I = 0$ (or $\cos'\alpha_I = 0$), the moment matrix $\mathbf{C}_t$ becomes singular as the values in the fourth (or sixth) column and row are all zero.

References

[1] W.T. Ang, B.I. Yun, A complex variable boundary element method for axisymmetric heat conduction in a nonhomogeneous solid, Appl. Math. Comput. 218 (2011) 2225–2236.
[2] P.H. Wen, M.H. Aliabadi, D.P. Rooke, Cracks in three dimensions: A dynamic dual boundary element analysis, Comput. Methods Appl. Mech. Eng. 167 (1998) 139–151.
[3] E. Schnack, H.B Chen, A multi-variable non-singular BEM in 2D elasticity, Eur. J. Mech.-A/Solids 20 (2001) 645–659.
[4] J.C.F. Telles, C.A. Brebbia, On the application of the boundary element method to plasticity, Appl. Math. Model. 3 (1979) 466–470.
[5] G.D. Manolis, P.K. Banerjee, Conforming versus non-conforming boundary elements in three-dimensional elastostatics, Int. J. Numer. Methods Eng. 23 (1986) 1885–1904.
[6] W.F. Florez, H. Power, Comparison between continuous and discontinuous boundary elements in the multidomain dual reciprocity method for the solution of the two-dimensional Navier–Stokes equations, Eng. Anal. Bound. Elem. 25 (2001) 57–69.
[7] P. Parreira, On the accuracy of continuous and discontinuous boundary elements, Eng. Anal. 5 (1988) 205–211.
[8] J.M. Zhang, X.Y. Qin, X. Han, G.Y. Li, A boundary face method for potential problems in three dimensions, Int. J. Numer. Methods Eng. 80 (2009) 320–337.
[9] X.Y. Qin, J.M. Zhang, G.Y. Li, X.M. Sheng, Q. Song, D.H. Mu, An element implementation of the boundary face method for 3D potential problems, Eng. Anal. Bound. Elem. 34 (2010) 934–943.
[10] M. Guiggiani, G. Krishnasamy, T.J. Rudolphi, F.J. Rizzo, A general algorithm for the numerical solution of hypersingular boundary integral equations, J. Appl. Mech. 59 (1992) 604–614.

[11] C.T. Dyka, H.R. Millwater, Formulation and integration of continuous and discontinuous quadratic boundary elements for two dimensional potential and elastostatics, Comput. Struct. 31 (1989) 495–504.
[12] J.M. Zhang, W.C. Lin, Y.Q. Dong, C.M. Ju, A double-layer interpolation method for implementation of BEM analysis of problems in potential theory, Appl. Math. Modell. 51 (2017) 250–269.
[13] J.M. Zhang, W.C. Lin, Y.Q. Dong, A dual interpolation boundary face method for elasticity problems, Eur. J. Mech.-A/Solids 73 (2019) 500–511.
[14] P. Lancaster, K. Salkauskas, Surfaces generated by moving least squares methods, Math. Comput. 37 (155) (1981) 141–158.
[15] G. Li, N.R. Aluru, Boundary cloud method: a combined scattered point/boundary integral approach for boundary-only analysis, Comput. Meth. Appl. Mech. Eng. 191 (2002) 2337–2370.
[16] G. Li, N.R. Aluru, A boundary cloud method with a cloud-by-cloud polynomial basis, Eng. Anal. Bound. Elem. 27 (2003) 57–71.
[17] D. Mirzaei, R. Schaback, M. Dehghan, On generalized moving least squares and diffuse derivatives, IMA J. Numer. Anal. 32 (2012) 983–1000.
[18] X.L. Li, S.L. Li, On the stability of the moving least squares approximation and the element-free Galerkin method, Comput. Math. Appl. 72 (2016) 1515–1531.
[19] M.A. Jaswon, Integral equation methods in potential theory. I, Proc. Royal Soc. Lond. Ser. A. Math. Phys. Sci. 275 (1963) 23–32.
[20] Y.J. Liu, N. Nishimura, The fast multipole boundary element method for potential problems: a tutorial, Eng. Anal. Bound. Elem. 30 (2006) 371–381.